

# Direct Growth of High Mobility and Low-Noise Lateral MoS<sub>2</sub>–Graphene Heterostructure Electronics

Amirhossein Behranginia, Poya Yasaei, Arnab K. Majee, Vinod K. Sangwan, Fei Long, Cameron J. Foss, Tara Foroozan, Shadi Fuladi, Mohammad Reza Hantehzadeh, Reza Shahbazian-Yassar, Mark C. Hersam, Zlatan Aksamija,\* and Amin Salehi-Khojin\*

**R**eliable fabrication of lateral interfaces between conducting and semiconducting 2D materials is considered a major technological advancement for the next generation of highly packed all-2D electronic circuitry. This study employs seed-free consecutive chemical vapor deposition processes to synthesize high-quality lateral MoS<sub>2</sub>–graphene heterostructures and comprehensively investigated their electronic properties through a combination of various experimental techniques and theoretical modeling. These results show that the MoS<sub>2</sub>–graphene devices exhibit an order of magnitude higher mobility and lower noise metrics compared to conventional MoS<sub>2</sub>–metal devices as a result of energy band rearrangement and smaller Schottky barrier height at the contacts. These findings suggest that MoS<sub>2</sub>–graphene in-plane heterostructures are promising materials for the scale-up of all-2D circuitry with superlative electrical performance.

## 1. Introduction

According to Moore's law, the transistor counts per chip doubles every two years.<sup>[1]</sup> The continuing shrinkage in size is pushing the silicon-based industry toward its physical limitations. Numerous efforts are now being dedicated to the development of 2D materials for future electronic/optoelectronic

devices.<sup>[2–8]</sup> Transition metal dichalcogenides (TMDs) are a family of layered crystals that are opening the possibility of developing systems with reduced dimensionality and a range of unique properties.<sup>[8]</sup> The most abundant member of this family is molybdenum disulfide (MoS<sub>2</sub>), which shows interesting semiconducting properties<sup>[9,10]</sup> that make it a promising candidate for digital electronic circuitry applications. On

A. Behranginia, P. Yasaei, Prof. M. R. Hantehzadeh, Prof. R. Shahbazian-Yassar, Prof. A. Salehi-Khojin  
Department of Mechanical and Industrial Engineering  
University of Illinois at Chicago  
Chicago, IL 60607, USA  
E-mail: salehikh@uic.edu

A. K. Majee, C. J. Foss, Prof. Z. Aksamija  
Electrical and Computer Engineering Department  
University of Massachusetts Amherst  
Amherst, MA 01003, USA  
E-mail: zlatana@engin.umass.edu

V. K. Sangwan, Prof. M. C. Hersam  
Department of Materials Science and Engineering  
Northwestern University  
Evanston, IL 60208, USA  
DOI: 10.1002/sml.201604301

Dr. F. Long  
Department of Mechanical Engineering  
University of Michigan Tech  
Houghton, MI 49931, USA  
T. Foroozan  
Department of Civil and Material Engineering  
University of Illinois at Chicago  
Chicago, IL 60607, USA  
S. Fuladi  
Department of Physics  
University of Illinois at Chicago  
Chicago, IL 60607, USA  
Prof. M. C. Hersam  
Department of Chemistry  
Northwestern University  
Evanston, IL 60208, USA



the downside, the electrical performance of MoS<sub>2</sub> field-effect transistors (FETs) has been limited by the performance of the MoS<sub>2</sub> junction with the metal contact electrodes.<sup>[11]</sup> In particular, due to Fermi level pinning, nearly all metals form a Schottky barrier upon contact with MoS<sub>2</sub>, which results in large contact resistances on the extrinsic (2-probe) performance of MoS<sub>2</sub>-based devices.<sup>[11]</sup> Additionally, metals do not possess sufficient mechanical bendability for use in flexible structures. Thus, significant research has been invested in finding a replacement for conventional metal electrodes that will allow the fabrication of intrinsically 2D devices with improved device metrics.<sup>[12–17]</sup>

In this study, we utilize seed-free consecutive CVD processes to synthesize lateral MoS<sub>2</sub>-graphene interfaces with large crystal domain sizes and high interface quality. Device-level experiments reveal that the extrinsic mobility of MoS<sub>2</sub>-graphene FETs is improved by an order of magnitude compared with the MoS<sub>2</sub>-metal FETs because of energy band rearrangement and smaller Schottky barrier height at the contacts, especially in the accumulation region (large positive gate voltages). For direct verification of the device-level measurements and to gain more insight into the role of the interface on the overall resistance of the device, Kelvin probe force microscopy (KPFM) is employed to map the surface potential distribution of a biased MoS<sub>2</sub>-graphene heterojunction under applied gate potentials. Low-frequency 1/f noise metrics of the MoS<sub>2</sub>-graphene FETs are also extensively studied in both subthreshold and accumulation

regions to identify the origins of signal fluctuations in lateral MoS<sub>2</sub>-graphene devices. The results show that the mobility fluctuations are the dominant origin of the noise in the accumulation region, while the overall noise amplitude is an order of magnitude lower than MoS<sub>2</sub>-metal FETs. Additionally, electrostatic breakdown measurements are performed on both MoS<sub>2</sub>-graphene and MoS<sub>2</sub>-metal devices to study the failure modes of the devices under high-power operation. To gain insight into the physics of the observed improvements, the interfacial resistance is modeled using a combination of first-principles band structure calculations, followed by calculation of the transmission coefficient and interfacial conductance in the Landauer formalism. Overall, this work establishes the superlative electronic properties of directly grown MoS<sub>2</sub>-graphene lateral heterostructures.

## 2. Results and Discussion

In our method, a graphene film with partial (or full) coverage is initially synthesized on a copper substrate in an atmospheric pressure chemical vapor deposition (AP-CVD) process and then transferred to a silicon (SiO<sub>2</sub>/Si) substrate, similar to our previous reports.<sup>[18,19]</sup> The samples are then transferred to another AP-CVD chamber to synthesize MoS<sub>2</sub> through the reaction of sulfur and molybdenum trioxide (MoO<sub>3</sub>) precursors. **Figure 1a,b** show the CVD-grown MoS<sub>2</sub> triangular single-crystalline flakes making a lateral junction

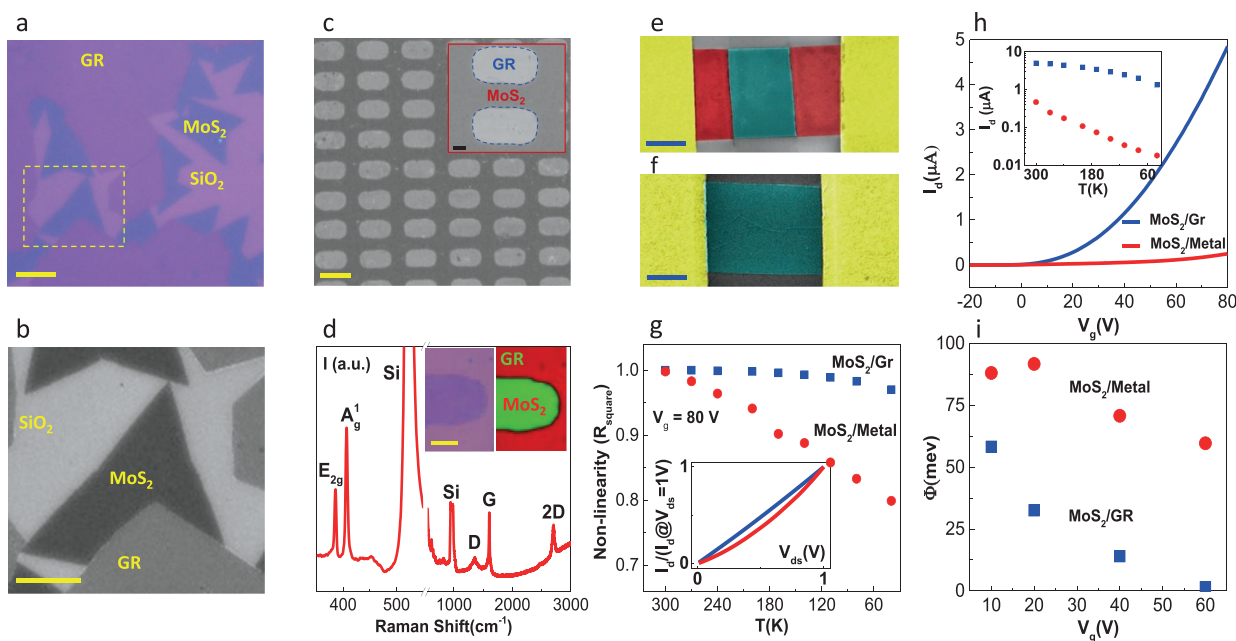


**Figure 1.** Characterization of the MoS<sub>2</sub>-graphene in-plane heterostructure. a) Optical image of the partially covered MoS<sub>2</sub> triangular flakes next to the graphene flakes (scale bar is 10 μm). b) SEM image of the MoS<sub>2</sub>-graphene in-plane heterostructure from the selected area in (a) (scale bar is 5 μm). c) SEM image of a large scale patterned MoS<sub>2</sub>-graphene in-plane heterostructure (scale bar is 10 μm), the inset magnifies the same image (scale bar in inset is 2 μm). d) A representative Raman point spectra from the MoS<sub>2</sub>-graphene interface area. The inset shows optical image and Raman mapping of a patterned MoS<sub>2</sub>-graphene heterostructure. The scale bar is 2 μm. e, f) SEM images of the MoS<sub>2</sub>-graphene and MoS<sub>2</sub>-metal FETs, respectively (scale bars are 2, and 1 μm, respectively). g) The linear regression ( $R_{\text{square}}$ ) of the  $I_d$ - $V_{ds}$  at different temperatures for the MoS<sub>2</sub>-graphene and MoS<sub>2</sub>-metal FETs (the inset shows normalized  $I_d$ - $V_{ds}$  characteristics of the both devices—normalized with their respective  $I_d$  at  $V_{ds} = 1$  V). h)  $I_d$ - $V_g$  characteristics of the MoS<sub>2</sub>-graphene and MoS<sub>2</sub>-metal FETs at 270 K (the inset shows the drain current at  $V_g = 80$  V with respect to temperature). i) Extracted Schottky barrier height—extracted from Arrhenius measurements—as a function of  $V_g$  for the MoS<sub>2</sub>-graphene and MoS<sub>2</sub>-metal FETs.

with graphene domains. The polycrystalline MoS<sub>2</sub> film is also grown next to the graphene flakes by increasing the MoS<sub>2</sub> growth time (Figure S1, Supporting Information). We note that even without any specific surface treatment (e.g., use of seed promoters), the growth of MoS<sub>2</sub> is more favorable on a bare oxide substrate compared to graphene films. This observation may be explained by the relative scarcity of nucleation sites on graphene compared to SiO<sub>2</sub>. The preferential deposition on SiO<sub>2</sub> causes the growth of MoS<sub>2</sub> to stop right at the edge of the graphene film, resulting in a lateral (in-plane) heterojunction. We note that due to the lattice mismatch between graphene and MoS<sub>2</sub>, an atomically sharp interface is not likely to form, but due to the self-limiting growth process (deposition selectivity), the overlapped region remains quite small (2–30 nm).<sup>[20]</sup> Atomic force microscopy (AFM) characterization (Figure S2, Supporting Information) also shows an overlapped region between MoS<sub>2</sub> and graphene domains, which is smaller than 30 nm over the entire interface length. We also found that a uniform MoS<sub>2</sub> film can fill arbitrary-shaped patterns in the graphene films and form lateral interfaces (Figure 1c). Raman point spectroscopy on a patterned MoS<sub>2</sub>–graphene interface shows the characteristic peaks of MoS<sub>2</sub> and graphene next to the silicon peaks from the substrate (Figure 1d). The inset of Figure 1d (right) shows the spatial distributions of the graphene and MoS<sub>2</sub> Raman peaks, which reveal the formation of a lateral interface without a noticeable gap or overlap. The classical least square (CLS) fitting was used to analyze the obtained hyperspectra, including the E<sub>g</sub><sup>2</sup> and A<sub>g</sub><sup>1</sup> peaks of the MoS<sub>2</sub> (coded as green in Figure 1d) and the G peak of the graphene (coded as red).

Next, we fabricated back-gated FETs by patterning metal electrodes on the graphene films rather than on the MoS<sub>2</sub> channel (Figure 1e,f). Figure S3 (Supporting Information) shows the two-probe current–voltage ( $I_d$ – $V_{ds}$ ) measurements at a back gate bias ( $V_g$ ) of 60 V for different temperatures. To compare the linearity of the  $I_d$ – $V_{ds}$  trends in the MoS<sub>2</sub>–graphene and MoS<sub>2</sub>–metal FETs, the normalized  $I_d$ – $V_{ds}$  trends (Y axis:  $I_d/I_{d@V_{ds}=1\text{ V}}$ ) at temperature 270 K are shown as an inset to Figure 1g. Unlike the MoS<sub>2</sub>–metal device, the MoS<sub>2</sub>–graphene FET shows a linear behavior. The correlation coefficient of the linear regression ( $R_{\text{square}}$ ) in the  $I_d$ – $V_{ds}$  is also calculated for both devices at different temperatures (see Figure 1g). The  $R_{\text{square}}$  of the MoS<sub>2</sub>–graphene FET starts from 1 at room temperature and goes to 0.970 at 40 K. However, the  $R_{\text{square}}$  of the MoS<sub>2</sub>–metal transistor shows greater temperature dependence (0.998–0.799). The larger nonlinearity in the  $I_d$ – $V_{ds}$  curve of the MoS<sub>2</sub>–metal device compared to the MoS<sub>2</sub>–graphene device—especially at low temperatures—suggests that a larger Schottky barrier is present for the metal-contacted MoS<sub>2</sub> device.

The output characteristics for both devices at different gate biases for different temperatures are also shown in Figure S4 (Supporting Information). Moreover, the electrical transfer characteristics ( $I_d$ – $V_g$ ) were measured at different temperatures (Figure S5, Supporting Information) and a typical n-type semiconducting behavior was obtained for both devices. The  $I_d$ – $V_g$  results at 270 K (Figure 1h) indicate that the current density ( $I_d \times \frac{L}{W}$ ) at  $V_g = 80$  V for the MoS<sub>2</sub>–graphene FET is 20 times higher than the MoS<sub>2</sub>–metal

FET. This ratio becomes even larger at low temperatures and approaches  $\approx 74$  times at 40 K (inset of Figure 1h), which is attributed to a smaller barrier for thermally induced charge carriers in the MoS<sub>2</sub>–graphene in-plane heterostructure. The extrinsic field-effect mobility is also calculated for both structures at room temperature and different back gate voltages (Figure S6a, Supporting Information). Both transistors are completely turned OFF at large negative gate biases and turned ON at a threshold voltage of 55 and 40 V with an ON/OFF ratio of 10<sup>4</sup> and 10<sup>5</sup> for MoS<sub>2</sub>–metal and MoS<sub>2</sub>–graphene, respectively. The linear field-effect mobility is calculated as  $\approx 11.5$  cm<sup>2</sup> V<sup>−1</sup> S<sup>−1</sup> for MoS<sub>2</sub>–graphene and  $\approx 1.5$  cm<sup>2</sup> V<sup>−1</sup> S<sup>−1</sup> for MoS<sub>2</sub>–metal at  $V_g = 80$  V. It should be noted that the field-effect mobility of the MoS<sub>2</sub>–metal devices is consistent with the previously reported mobility of monolayer CVD grown MoS<sub>2</sub> without top-gate dielectrics.<sup>[13]</sup> However, higher extrinsic mobility values can be achieved by using multilayer MoS<sub>2</sub><sup>[21]</sup> or using high-k dielectric substrates/overcoats.<sup>[22]</sup> Our temperature-dependent measurements show that the mobility of the MoS<sub>2</sub>–metal FET is reduced by 95% as the temperature is decreased to 40 K, while the MoS<sub>2</sub>–graphene FET shows almost constant mobility down to 160 K and then 30% reduction in the mobility at 40 K (Figure S6b, Supporting Information). This temperature dependence is also demonstrated in the inset of Figure 1h in which the drain current of the MoS<sub>2</sub>–graphene device reduces by  $\approx 4$  times, while that of the MoS<sub>2</sub>–metal device decreases by  $\approx 26$  times.

To gain better insight concerning the Schottky barrier height, a 2D thermionic model is used to analyze the data.<sup>[23]</sup> Figure S7 (Supporting Information) shows the logarithmic plots of ( $I_d/T^{3/2}$ ) versus ( $1000/T$ ) for the MoS<sub>2</sub>–graphene and MoS<sub>2</sub>–metal interfaces at different  $V_{ds}$  and different back gate biases (Sections 7–9, Supporting Information). In Figure S9 (Supporting Information), a switch in the sign of the slope at  $V_g \cong 60$  V reveals the absence of the Schottky barrier for the MoS<sub>2</sub>–graphene in-plane contact at large gate voltages. Figure 1i further shows the derived Schottky barrier height of both structures at room temperature for different applied gate voltages. The Schottky barrier height for the MoS<sub>2</sub>–metal structure is about 88 meV at  $V_g = 10$  V and decreases to 60 meV for  $V_g = 60$  V, while the MoS<sub>2</sub>–graphene in-plane heterostructure starts at  $\approx 58$  meV at  $V_g = 10$  V and fades to zero at  $V_g = 60$  V.

We also performed KPFM experiments to map the surface potential distribution across the MoS<sub>2</sub>–graphene interface under applied source–drain and gate voltages (setup is shown Figure S10, Supporting Information). This technique enables us to spatially map the local potential drops in the MoS<sub>2</sub>–graphene lateral heterojunction and in the MoS<sub>2</sub> and graphene films under device operational conditions to gain insight into their relative contributions to the overall resistance of the device. **Figure 2a** shows the KPFM mapping of the device at  $V_{ds} = 0$  V and  $V_g = 0$  V. We also mapped the change in the surface potential along the entire length of the device at  $V_{ds} = 1$  V and at different gate voltages (Figure 2b,c). As the gate voltage increases from  $-20$  to  $+20$  V, the potential drop across the interface decreases from 455 to 201 mV (Figure 2d). This observation implies that the contribution of the resistive potential drop across the interface relative to

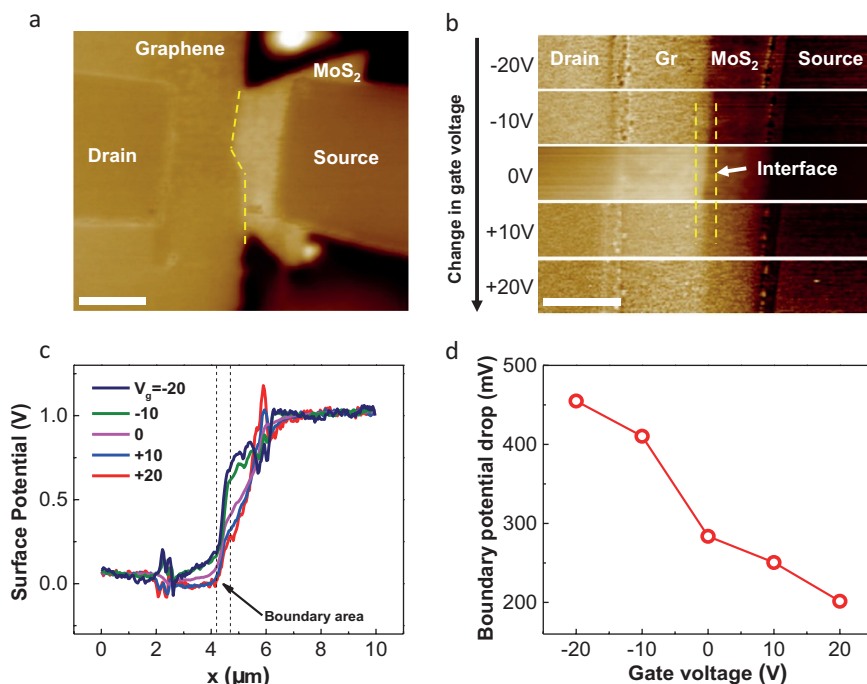


**Figure 2.** KPFM measurements. a) KPFM mapping of the MoS<sub>2</sub>–graphene transistor with  $V_{\text{gate}} = 0$  V and  $V_{\text{ds}} = 0$  V. The interface between graphene and MoS<sub>2</sub> is highlighted with yellow dashed line (scale bar is 2  $\mu\text{m}$ ). b) KPFM mapping of the interface area from a selected region shown in (a) by keeping  $V_{\text{ds}} = 1$  V and changing  $V_{\text{gate}}$  from  $-20$  to  $+20$  V with 10 V increments (scale bar is 2  $\mu\text{m}$ ). The dashed lines show the interface area. c) Corresponding surface potential profiles across the interface area. d) The potential drop at the interface area as a function of the applied gate voltages.

the total resistance of the device decreases as one increases the gate voltage. In other words, the MoS<sub>2</sub>–graphene contact resistance has a negligible contribution to the overall device resistance at larger gate voltages.

Next, a systematic study of  $1/f$  noise was performed in the MoS<sub>2</sub>–graphene and MoS<sub>2</sub>–metal devices in a vacuum (pressure  $< 10^{-5}$  Torr). Low frequency  $1/f$  noise has the potential to severely limit the performance of nanoscale materials because  $1/f$  noise increases with decreasing number of carriers (i.e., device size). Recently, it has been shown that metal contacts can play a significant role in  $1/f$  noise in CVD-grown MoS<sub>2</sub>. Thus,  $1/f$  noise is an important metric to gauge the quality and viability of lateral graphene–MoS<sub>2</sub> heterojunctions. Regardless of the fundamental sources of  $1/f$  noise (i.e., mobility fluctuation versus carrier number fluctuation), the noise power spectral density  $S_I$  can be described empirically as:

$$S_I = \frac{AI^\gamma}{f^\beta} \quad (1)$$

where  $I$  is mean drain current,  $f$  is frequency,  $A$  is noise amplitude, and exponents  $\beta$  and  $\gamma$  are expected to be close to ideal values of 1 and 2, respectively. **Figure 3a** shows  $1/f^\beta$  dependence of noise spectral density for a MoS<sub>2</sub>–graphene device with  $\beta = 1.02 \pm 0.002$  over four decades of frequency. For more thorough analysis, the noise measurement was limited to 1–100 Hz and  $\beta$  was found to be in the range  $1.0 \pm 0.2$  for all measured devices. In our tests,  $S_I \sim I^\gamma$  where  $\gamma = 1.6$ –2.1 for all measured devices, confirming that  $1/f$  noise is caused

by fluctuations in the resistance (Figure S11a, Supporting Information).

We also studied the gate-dependence of  $1/f$  noise characteristics to understand the origins of the low-frequency fluctuations and the relative role of contacts in MoS<sub>2</sub>–graphene and MoS<sub>2</sub>–metal devices. **Figure 3b** shows  $1/f$  behavior of a MoS<sub>2</sub>–graphene device for  $V_g = -40$  to 70 V. Noise spectral density shows  $1/f^\beta$  behavior ( $\beta = 0.97$ –1.2) with no clear dependence on  $V_g$  over the whole range (see inset of **Figure 3c**). Transfer characteristics ( $I_d$ – $V_g$ ) of this device show a threshold voltage  $V_{\text{th}} = 40$  V (**Figure 3c**), and thus measurements cover both accumulation ( $V > V_g - V_{\text{th}}$ ) and subthreshold regions ( $V < V_g - V_{\text{th}}$ ). The noise amplitude  $A$  was extracted from the plots of  $I^2/S_I$  versus frequency with the  $V_g$  dependence analyzed in **Figure 3c,d**. First,  $1/A$  varies linearly with  $V_g$  in the accumulation region (**Figure 3c**), even though  $I_d$  follows a superlinear behavior with  $V_g$  in accumulation. Note that  $I \sim V_g^m$  ( $m = 1$ –2) behavior arises from reduced screening effect in a 2D material with parabolic band structure and has been described in experimental findings<sup>[24]</sup> and in ana-

lytical calculations.<sup>[25]</sup> Within Hoooge’s mobility fluctuation model, the noise amplitude  $A$  is related to the carrier number ( $N$ ) according to  $A = \alpha_H/N$ , where  $\alpha_H$  is Hoooge’s parameter and  $N = C_g/(V_g - V_{\text{th}})/q$  in the accumulation region, where  $C_g$  is total gate oxide capacitance and  $q$  is an electronic charge. Thus, the linear  $1/A \sim V_g$  dependence in the accumulation regime in **Figure 3c** and strong correlation between noise amplitude and current throughout the whole range of  $V_g$  suggests mobility fluctuation or correlated mobility-number fluctuation as the dominant source of current fluctuations in the accumulation region, in agreement with previous  $1/f$  noise studies conducted on exfoliated MoS<sub>2</sub> transistors.<sup>[26]</sup> The number fluctuation model predicts the correlation between  $A$  and  $(g_m/I)^2$ , where  $g_m$  is the transconductance.<sup>[27–30]</sup> In the absence of such correlation in these devices, we rule out the number fluctuation model. The Hoooge parameter for this device was extracted as  $\alpha_H = 0.21$ , which is comparable to previous CVD-grown MoS<sub>2</sub><sup>[31]</sup> but larger than high quality exfoliated MoS<sub>2</sub> by up to two orders of magnitude.<sup>[26]</sup> Indeed, the average Hoooge parameter of six measured devices is  $0.33 \pm 0.08$ .

Now we consider the role of contacts in the  $1/f$  noise behavior in graphene–MoS<sub>2</sub> and metal–MoS<sub>2</sub> devices. In the case of significant Schottky barriers at the contacts, fluctuations in both channel resistance ( $R_{\text{ch}}$ ) and contact resistance ( $R_c$ ) can contribute to the overall noise in the transistor. Thus, the normalized noise spectral density can be written as:

$$\frac{S_I}{I^2} = \frac{S_{R_c}}{R_c^2} \frac{R_c^2}{(R_{\text{ch}} + R_c)^2} + \frac{S_{R_{\text{ch}}}}{R_{\text{ch}}^2} \frac{R_{\text{ch}}^2}{(R_{\text{ch}} + R_c)^2} \quad (2)$$

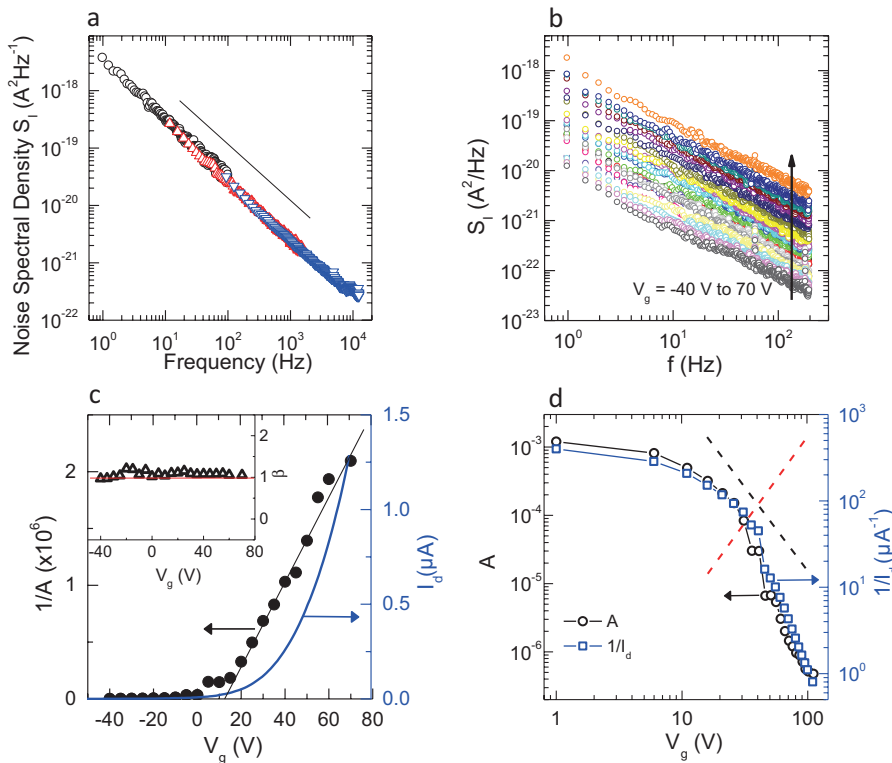


**Figure 3.**  $1/f$  noise measurements of MoS<sub>2</sub>-graphene and MoS<sub>2</sub>-metal FETs. a) Noise spectral density ( $S_1$ ) as a function of frequency for a MoS<sub>2</sub>-graphene FET at  $V_g = 60$  V and  $V_{ds} = 4$  V showing  $1/f^\beta$  behavior with  $\beta = 1.02 \pm 0.002$ . The black line shows ideal  $1/f$  behavior. b)  $S_1$  versus frequency of the device at  $V_g$  varying from  $-40$  to  $70$  V at  $V_{ds} = 2$  V. c) Inverse of noise amplitude ( $1/A$ ) versus  $V_g$  compared with transfer characteristics (device current ( $I_d$ ) versus  $V_g$ ) from the data in (c). The inset shows  $\beta$  as a function of  $V_g$ . d) Log-log plot of  $A$  and  $1/I_d$  versus  $\Delta V_g (=V_g + 41)$  where  $V_g$  is ranging from  $-40$  to  $70$  V. Black and red dashed lines show  $V_g^{-2}$  and  $V_g^2$  dependence for purely channel and purely contact effects on  $1/f$  noise, respectively.

where  $S_{Rc}$  and  $S_{Rch}$  are power spectral density originating solely from the contacts and the channel, respectively. Based on this equation for the number fluctuation model, in the case of dominant channel resistance, noise  $A$  (and  $S_1/P^2$ ) would vary as  $\approx V_g^2$ , and in the case of dominant contact resistance, the noise would result in  $\approx V_g^{-2}$  dependence in the accumulation region. In our results,  $A$  versus  $V_g$  behavior follows  $V_g^m$  ( $m = 1-2$ , see Figure S11b in the Supporting Information). Note that a log-log plot of  $A$  versus  $\Delta V_g$  overestimates the exponent  $m$  in Figure 3d. However, the  $A$  versus  $V_g$  behavior is starkly different from the  $\sim V_g^2$  behavior expected for dominant contact resistance that has been seen in previous CVD-grown MoS<sub>2</sub> transistors.<sup>[29]</sup> Thus, we can conclude that the MoS<sub>2</sub>-graphene interface is not the dominant source of  $1/f$  noise in our devices.

Now we discuss control MoS<sub>2</sub>-metal devices and directly compare the noise metrics between two kinds of devices. Noise spectral density follows  $I^{\gamma}/f^{\beta}$  behavior in all MoS<sub>2</sub>-metal devices with exponent  $\beta = 1 \pm 0.2$  and  $\gamma = 2 \pm 0.3$  (Figure S12a,b, Supporting Information).  $1/A$  dependence on  $V_g$  is also linear in the accumulation region, suggesting the validity of the mobility fluctuation model (Figure S12c, Supporting Information). The average Hooge parameter for four measured MoS<sub>2</sub>-metal devices was found to be  $4.59 \pm 2.58$ , an order of magnitude higher than MoS<sub>2</sub>-graphene devices.

Note that the Hooge parameter of the present MoS<sub>2</sub>-metal devices is higher than values reported in the literature on CVD-grown MoS<sub>2</sub>.<sup>[32]</sup> However, the present MoS<sub>2</sub>-graphene and MoS<sub>2</sub>-metal devices use MoS<sub>2</sub> grown under identical conditions and undergo the same processing steps. Thus, reduced noise could be correlated to superior contact (as shown by transport and KPFM experiments) in lateral MoS<sub>2</sub>-graphene devices. Further evidence of larger current fluctuations is seen in Figure S12d (Supporting Information), which shows a dip in  $1/A$  versus  $V_g$  behavior for some MoS<sub>2</sub>-metal devices. Such a peak has been seen before in bilayer MoS<sub>2</sub> and V, M, and  $\Lambda$ -shaped noise dependence on carrier density in single- and few-layer graphene.<sup>[33,34]</sup> Thus, the dip in  $1/A$  can be explained within a model that takes into account the van der Waals gap between MoS<sub>2</sub> and traps inside SiO<sub>2</sub> that results in noise increasing with  $N$  at low  $N$  and decreasing with  $N$  at high  $N$ . Overall, the absence of such a dip in MoS<sub>2</sub>-graphene devices suggests lower disorder possibly from the contacts.

Finally, we compare the normalized noise amplitude ( $A \sim 1/N$ ) with the total number of carriers (i.e., channel area  $L \times W$ ) for all measured MoS<sub>2</sub>-graphene and MoS<sub>2</sub>-metal devices (Figure 4).  $V_g$  dependence of normalized noise amplitude shows overall decreased noise in MoS<sub>2</sub>-graphene. Furthermore, channel area scaling results in a tighter distribution

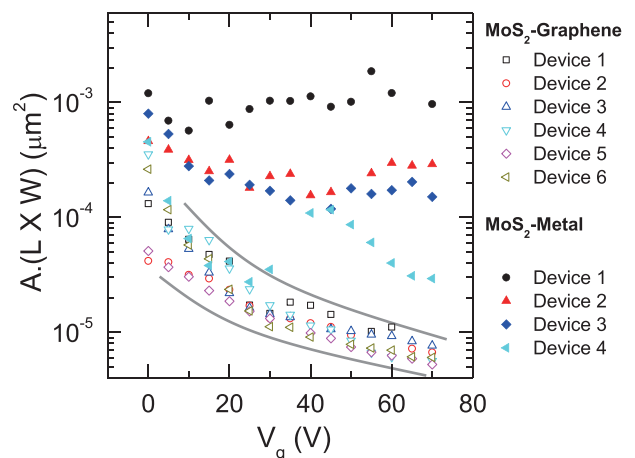


**Figure 4.** Comparison of area-normalized noise amplitude ( $A \cdot (L \times W)$ ) of MoS<sub>2</sub>-graphene and MoS<sub>2</sub>-metal FETs as a function of  $V_g$ . Two gray lines show upper and lower bounds of noise amplitude for MoS<sub>2</sub>-graphene devices.

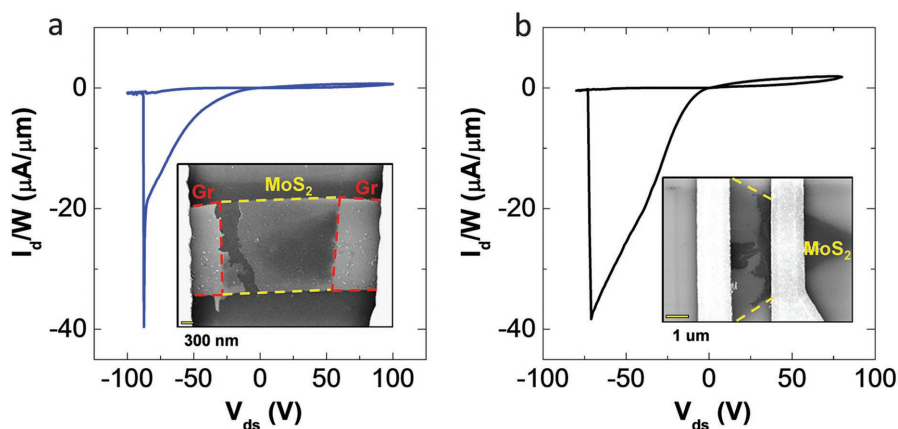


**Figure 5.** Breakdown study of MoS<sub>2</sub>-graphene and MoS<sub>2</sub>-metal FETs. a,b) Current-voltage characteristics of a MoS<sub>2</sub>-graphene and MoS<sub>2</sub>-metal FET, respectively, at  $V_g = 0$  V showing irreversible breakdown at large  $V_{ds}$ . The current was normalized to the channel width. The insets of Figure (a) and (b) show scanning electron microscopy micrographs of the MoS<sub>2</sub>-graphene and MoS<sub>2</sub>-metal FETs after the breakdown, respectively.

of noise metrics for MoS<sub>2</sub>-graphene devices (Figure 4), suggesting MoS<sub>2</sub>-metal has a larger contribution of noise from the contacts. Furthermore, the overall  $V_g$  dependence is more well-defined ( $A \sim 1/V_g$ ) in MoS<sub>2</sub>-graphene devices, again corroborating the dominance of channel resistance fluctuations compared to contact resistance fluctuations.

For reliable electronics, it is also critical to achieve mechanically and electrostatically robust contacts. The present MoS<sub>2</sub>-graphene devices have essentially a 1D interface between two 2D materials. Thus far, electrostatic breakdown of a lateral heterojunction of this type has not been probed. **Figure 5a,b** shows current-voltage characteristics of a MoS<sub>2</sub>-graphene and a MoS<sub>2</sub>-metal device for  $V_{ds} = 75$  to  $-75$  V (sweep rate =  $1$  V s<sup>-1</sup>) under vacuum (pressure <  $10^{-5}$  torr). Both devices show qualitatively similar behavior of electrostatic breakdown. In particular, the current decreases irreversibly by more than two orders of magnitude within 1 V. Interestingly, both MoS<sub>2</sub>-graphene and MoS<sub>2</sub>-metal devices show comparable maximum width-normalized drain current ( $\approx 40$   $\mu\text{A } \mu\text{m}^{-1}$ ) just before breakdown, roughly an order of magnitude lower current density than high quality exfoliated monolayer MoS<sub>2</sub>.<sup>[35]</sup> The breakdown field of the two devices is also comparable ( $\approx 38$  MV m<sup>-1</sup>). Scanning electron microscopy of the broken devices was conducted to probe morphological evidence of the failure mode (inset of Figure 5a,b). A significant portion of MoS<sub>2</sub> was found missing near the drain contacts in both of the devices. This suggests a similar failure mechanism irrespective of metal or lateral graphene contacts. Thus, direct growth of the MoS<sub>2</sub>-graphene heterojunction does not significantly affect the electrostatic breakdown characteristics of the devices.

To shed light on the origin of the improved electrical performance of the MoS<sub>2</sub>-graphene devices, we perform bandstructure, band alignment, and transport calculations. The total resistance ( $R_{\text{tot}}$ ) of the device between source and drain is comprised of the series resistances from the graphene grains ( $R_{\text{grap}}$ , forming source and drain), resistance of MoS<sub>2</sub> grain ( $R_{\text{MoS}_2}$ , constituting the channel), and resistances of the interfaces ( $R_{\text{int}}$ ) between graphene and MoS<sub>2</sub>. We

calculate the series grain resistances of graphene and MoS<sub>2</sub> sections from the general expression— $R_{2D} = \rho \frac{L}{W}$ , where  $\rho$  is the resistivity of the material (sheet resistance in this case) and  $\frac{L}{W}$  is the aspect ratio of the sample. The conductivity ( $\sigma = \frac{1}{\rho}$ ) of graphene and MoS<sub>2</sub> grain is calculated from  $\sigma = qn\mu$ , where  $n$  is the sheet charge density,  $\mu$  is the carrier mobility (mobility calculation is further elaborated in the Experimental Section).

The calculation of interface resistance involves four steps: bandstructure calculations for each graphene and MoS<sub>2</sub> from first principles, band alignment at the interface based on the Schottky-Mott rule, calculation of electron transmission across the interface from energy and momentum conservation at the interface, and finally computing the interface resistance in the Landauer formalism.

Density functional theory (DFT) supercell calculations are widely used in the literature for vertical heterostructures as well as lateral heterostructures<sup>[36,37]</sup> formed by more commensurate materials like hBN-graphene. However, performing extended supercell calculations for lateral interfaces formed by highly incommensurate materials such as graphene-MoS<sub>2</sub> becomes computationally very expensive.<sup>[38]</sup> In this work, we first calculate the electronic band structure of graphene and MoS<sub>2</sub> individually using first-principles DFT as implemented within the open-source distribution Quantum-Espresso<sup>[39]</sup> (further details on the DFT calculations are given in the Experimental Section). The calculated band structures and densities of states (DOS) are shown in Figure S13a,b (Supporting Information), respectively. Then we align the bands at the interface using a semiclassical Schottky-Mott rule, where the vacuum levels are matched at the interface and bands are aligned using their respective electron affinities and work functions. Several papers show that band alignment in 2D lateral heterojunctions follows the Schottky-Mott rule and that the band alignment is relatively insensitive to the interfacial details when the overall dimensions of the device are much larger than the characteristic junctions width<sup>[38,40,41]</sup> as is the case in our samples. The difference in work function ( $\phi$ ) and the electron affinity ( $\chi$ ) of graphene and MoS<sub>2</sub> results in the formation of an energy barrier ( $\phi_B$ ) at the interface. As graphene is essentially metallic, the bands bend only on the MoS<sub>2</sub> side near the interface to account for the energy barrier height. The resulting band structure alignment at the interface for zero gate voltage is shown in Figure S13 (Supporting Information). Further details on how the two band structures are aligned at the interface under extrinsic (gated) conditions are given in Figure S14 (Supporting Information).

On aligning the bands at the interface, we developed a numerical model to calculate the transmission coefficient of electrons over the energy barrier from graphene to MoS<sub>2</sub>. In our model, we include both the effect of the potential barrier at the interface and the mismatch in the electronic band

structures of the two materials by simultaneously conserving the energy as well as the component of the wavevector parallel to the interface. This approach, which is an extension of the method originally proposed by Yazyev and Louie<sup>[42]</sup> for electron transmission through graphene–graphene grain boundaries, allows us to calculate the dependence of interfacial resistance between graphene and MoS<sub>2</sub> on the band alignment between the two domains at the heterojunction. Momentum conservation requires that the parallel component of the incident wave vector ( $k_{\parallel}$ ) be equal to the parallel component of the transmitted wave vector ( $k_{\parallel}$ ), in their respective domains; simultaneously, energy is conserved by finding a perpendicular component of the transmitted wave vector ( $k_{\perp}$ ), within the first Brillouin zone of MoS<sub>2</sub>, such that  $E_1(k_{\parallel}) = E_2(k_{\parallel} + k_{\perp})$ . The mode-dependent transmission coefficient is then calculated using the perpendicular components of the incident ( $k_{\perp}$ ) and transmitted ( $k_{\perp}$ ) wave vectors using a general expression for wave transmission between two domains<sup>[43]</sup> are given by  $\tau_b(k_{\parallel}) = \frac{4k_{\parallel} k_{\perp}}{|k_{\parallel} + k_{\perp}|^2}$ , where  $b$  represents the electron band. Finally, we obtain the energy-resolved values of the transport distribution function (TDF),  $\Xi(E)$ , from the transmission coefficient and velocity as  $\sum_b v_b(E)\Gamma_b(E)D_b(E)$ , where  $D_b(E)$  represents density of states of the  $b_{th}$  band, by averaging the product of transmission coefficient  $\tau_b(k)$  and electron group velocity  $v_b(k)$  over the

constant energy contour,  $\delta(E - E_b(k))$ , using the 2D version of the linear extrapolation approach described by Gilat and Raubenheimer<sup>[44]</sup> and then summing it over all electron bands (b):

$$\begin{aligned} \Xi(E) &= \sum_b v_b(E)\Gamma_b(E)D_b(E) \\ &= \sum_b \frac{1}{4\pi^2} \int v_b(k)\tau_b(k)\delta(E - E_b(k))dk \end{aligned} \quad (3)$$

The TDF is then used to numerically calculate the interfacial conductance in the Landauer formalism and inverted to obtain the interfacial resistance  $R_{int}$ , as:

$$R_{int}^{-1} = G_{int} = \frac{q^2}{2} \int_{E_c}^{E_{max}} \Xi(E) \left( -\frac{\partial f(E - E_F, T)}{\partial E} \right) dE \quad (4)$$

where  $E_c$  is the bottom of the conduction band,  $E_{max}$  is the highest electron energy among the bottom four conduction bands and  $f(E)$  is the Fermi-Dirac distribution function,  $f(E) = [1 + \exp(E - E_F/k_B T)]^{-1}$ .

In the case of a finite gate voltage and zero drain bias, the Fermi levels in both graphene and MoS<sub>2</sub> away from the interface shift relative to their position at zero gate voltage in response to the induced charge in the 2D layers, as shown in **Figure 6a**. Consequently, the energy bands on both sides

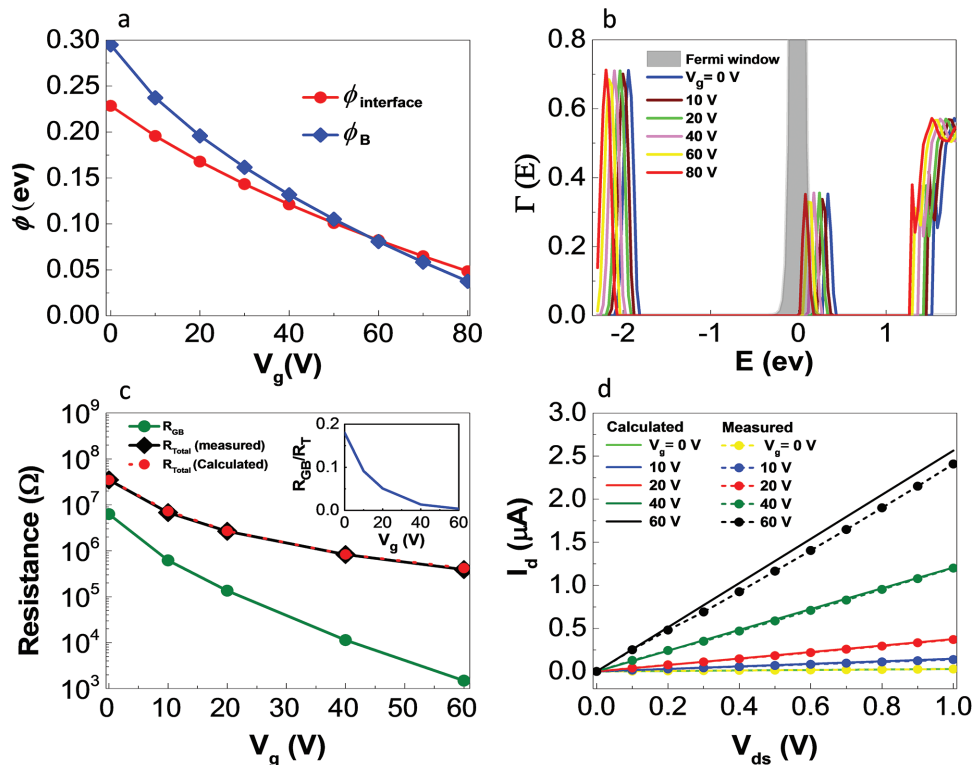


**Figure 6.** a) Variation in interfacial Schottky potential barrier height—from graphene to MoS<sub>2</sub> ( $\phi_B$ ) and from MoS<sub>2</sub> to graphene ( $\phi_{interface}$ )—with gate voltage ( $V_g$ ). b) Resulting shift in transmission coefficient with gate voltage, such that with the increasing  $V_g$  a larger part of  $\Gamma(E)$  overlaps with the Fermi window (shown by the grey area in the plot) resulting in increased conductance. c) Interfacial resistance ( $R_{int}$ ) and the total resistance ( $R_{tot}$ )—both measured (red line with red markers) and calculated (black line with black markers)—against gate voltage. The inset shows the percentage contribution of interfacial resistance ( $R_{int}$ ) towards the total resistance ( $R_{tot}$ ) of the device at different gate voltages, in good agreement with KPFM measurements. d) Drain current ( $I_d$ ) versus drain-source voltage ( $V_{ds}$ ) calculated both experimentally and by numerical simulation showing good agreement between numerical and experimental results.

of the interface rearrange themselves to maintain the equilibrium condition. However, the shift in the bands on the two sides is not identical because the two materials have different DOS (Figure S13b, Supporting Information), leading to an increase in band bending in the MoS<sub>2</sub> with increasing gate bias. The transmission coefficient of electrons across the interface, however, depends on the alignment of energy bands of graphene and MoS<sub>2</sub> at the interface. For example, states near the Fermi level in graphene cannot typically be transmitted because there are no available states at the same energy in MoS<sub>2</sub> as energies near the Fermi level fall inside the bandgap. Increasing the gate bias increases the sheet charge density in both graphene and MoS<sub>2</sub>; in response, the barrier height at the junction of the two domains decreases with increasing gate voltages (Figure 6a), in agreement with the electrical measurements in Figure 1i.

As a result of band rearrangement and barrier lowering, the transmission  $\Gamma(E)$  also shows a dependence on gate voltages. It can be seen in Figure 6b that with increasing gate voltages, the transmission coefficient  $\Gamma(E)$  shifts toward the left resulting in a larger overlap between  $\Gamma(E)$  and the so-called Fermi window  $\left(-\frac{df}{dE}\right)$ , centered at the Fermi level. An increase in overlap between the transmission  $\Gamma(E)$  and the Fermi window corresponds to a reduction in interfacial resistance. In addition to the reduction in interfacial resistance with gate voltage, we obtain a reduction in the resistance of the MoS<sub>2</sub> due to the increase in sheet charge density and mobility with gate voltage (conductance calculation described further in Experimental Section). The simultaneous reduction in interfacial resistance and MoS<sub>2</sub> resistance with gate bias leads to an overall decrease in the total resistance ( $R_{\text{tot}}$ ), as can be seen in Figure 6c. We find that the contribution of the interfacial resistance to the total resistance of the combined MoS<sub>2</sub>+interface+graphene system ( $R_{\text{tot}}$ ) decreases with increasing gate voltages, starting at around 25% of the total in the intrinsic case (zero gate bias), and rapidly dropping below 1% at gate voltage of 60 V, as shown in the inset of Figure 6c, further corroborating the KPFM measurements at the interface. The agreement between measured and calculated total resistances of the device, mathematically written as  $R_{\text{tot}} = 2R_{\text{grap}} + R_{\text{MoS}_2} + 2R_{\text{int}}$  and shown in Figure 6d, indicates that the measured resistances are well reproduced by the model. We also show that at large non-zero gate biases, the interface contributes very little to the overall resistance, leading to Ohmic behavior.

### 3. Conclusion

A seed-free synthesis of graphene and MoS<sub>2</sub> lateral heterojunctions through the CVD method is reported, which exhibit improved electrical performance compared to conventional metal-contact MoS<sub>2</sub> devices. This method makes in-plane MoS<sub>2</sub>-graphene heterostructures promising for the large-scale production of electronic and logic circuits from all-2D materials for next generation device applications. Temperature-dependent electrical characterization shows Ohmic behavior for the MoS<sub>2</sub>-graphene FET devices at back-gate voltages above 60 V, verifying a high-quality lateral interface between

MoS<sub>2</sub> and graphene. KPFM results also visualize the reduction of the MoS<sub>2</sub>-graphene in-plane junction resistance at positive gate voltages. We further present the first study of  $1/f$  noise in 2D lateral heterojunction electronic circuits. MoS<sub>2</sub>-graphene devices show up to an order of magnitude lower noise amplitude in comparison to MoS<sub>2</sub>-metal devices fabricated under similar conditions. A systematic study of  $1/f$  noise by varying gate bias and area-scaling revealed the dominant origin of noise as mobility fluctuations in the accumulation region. We also conducted the first electrostatic breakdown study of lateral MoS<sub>2</sub>-graphene heterojunctions. In this case, MoS<sub>2</sub>-graphene and MoS<sub>2</sub>-metal devices showed comparable current density, breakdown fields, and similar failure modes through microscopic visualization. Our numerical calculations reveal that both the barrier at the interface as well as the resulting interfacial resistance decrease as sheet charge is increased in response to the external gate voltage, matching the KPFM results. At gate voltages above 60 V, the interface contributes less than 1% to the overall device resistance despite the appreciable electron mobility in MoS<sub>2</sub>, resulting in the observed linear (Ohmic) behavior.

### 4. Experimental Section

*Graphene Growth Procedure:* The three-zone MTI CVD furnace<sup>[45]</sup> was used for graphene growth. The partially and fully covered graphene films were grown on the copper substrate (Alfa Aesar, product no. 46365) by using atmospheric pressure CVD growth process. The copper substrate was immersed inside of the hydrochloric acid for 15 min to remove the local surface oxides and then rinsed with acetone and isopropanol. Next, the copper substrate was placed inside of the CVD furnace and then the chamber was evacuated to the 1 mTorr vacuum pressure to remove the unwanted gasses. The chamber was then restored to atmospheric pressure by filling it with 5% hydrogen diluted in argon gas. The growth procedure consists of three main steps. The first step was annealing, in which the maximum temperature of the furnace is set to 1050 °C and the annealing time was 1 h for the growth of both partially and fully covered graphene films. In the second step, the furnace was filled with 20 p.p.m methane gas and the growth time was 60 min for partial coverage graphene and 90 min for full coverage graphene film. The third step was cooling in which the furnace was cooled down to room temperature by force cooling and the methane gas also was stopped from flowing into the furnace.

*Growth Process of CVD MoS<sub>2</sub> on Graphene/SiO<sub>2</sub>/Silicon Substrate:* The oxygen plasma treatment was performed on SiO<sub>2</sub>/Silicon substrate for 2 min to make the substrate hydrophilic, which helps with the transfer of the graphene film and the growth of MoS<sub>2</sub> on the substrate. After transferring the partial coverage graphene film onto the SiO<sub>2</sub>/silicon substrate, the substrate was annealed at 400 °C for 8 h. The 5% diluted hydrogen in argon gas was also continuously supplied during the annealing process to remove the residue of the transfer process. Then, the substrate was placed inside of the MoS<sub>2</sub> CVD chamber together with 2 mg of molybdenum tri-oxides and 1 g of sulfur as precursors for the MoS<sub>2</sub> growth. The chamber temperature increased to 550 °C in 30 min and then it was increased to 850 °C in 60 min. The growth time was 10 min and then furnace was cooled down to the room temperature by

natural cooling. It is worth mentioning that increasing the time of the MoS<sub>2</sub> growth or the amount of the MoO<sub>3</sub> powder will result in the growth of the MoS<sub>2</sub> film on top of the graphene film.<sup>[46]</sup>

**Fabrication of the MoS<sub>2</sub>-Graphene Field Effect Transistors:** After the graphene film was transferred onto the SiO<sub>2</sub> substrate, it was patterned into rectangles by a photolithography process followed by oxygen plasma etching. Next, MoS<sub>2</sub>-graphene heterostructure was synthesized, and the metal electrodes were patterned on the MoS<sub>2</sub>-graphene FETs and on the MoS<sub>2</sub> FETs by an electron beam lithography method. Finally, 10 nm titanium and 60 nm gold were deposited on the devices by an electron beam evaporation process.

**KPFM:** All AFM experiments were carried out with a dimension ICON system (Bruker, CA) in ambient conditions. PFQNE-AL cantilevers (Bruker, CA) were selected for improved spatial resolution in surface potential measurements. The nominal spring constant is 0.8 N m<sup>-1</sup> and the resonant frequency is 300 kHz. Two-pass technique (also known as “lift mode”) was applied in KPFM experiments. During scanning, the sample was grounded, while a bias  $\Delta V = V_{DC} + V_{AC}$  was applied to the AFM cantilever, where the  $V_{DC}$  and  $V_{AC}$  are the DC and AC component, respectively. The frequency of  $V_{AC}$  was chosen at the resonant frequency of the cantilever. The AFM controller nulled the cantilever amplitude due to periodic electrostatic force by adjusting  $V_{DC}$ . If the work function of the cantilever tip  $\Phi_{tip}$  is known, then the sample work function  $\Phi_s$  can be given as  $\Phi_s = \Phi_{tip} - eV_{DC}$ .  $\Phi_s$  and  $V_{DC}$  are opposite in sign, so the work function  $\Phi_s$  has inverse contrast with KPFM mapping. All AFM data were analyzed with Nanoscope Analysis software (Bruker, CA).

**1/f Noise and Breakdown Measurements:** All 1/f noise and breakdown measurements were carried out under vacuum (pressure  $\approx 10^5$  torr) using a LakeShore CRX 4K probe station. The current fluctuations were amplified with a low-noise voltage amplifier (DL Instruments 1212) and power spectral density was captured with a spectrum analyzer (Stanford Research SR780). Drain and gate voltage were controlled by Keithley Instruments 2400 source meters and homemade LabView programs. Power spectral density in devices powered by stand-alone batteries and source-meters was found to be comparable, thus confirming that the measurement apparatus does not contribute to the measured noise.

**Raman Mapping:** The Swift mode Raman mapping with a 500 nm scanning step size was performed for two different ranges with the total number of 1824 collected spectra. The first range was from 100 to 900 cm<sup>-1</sup> and the second one was from 800 to 1700 cm<sup>-1</sup>. The classical least-square fitting was used to analyze the Raman data, which includes the E<sub>2g</sub> and A<sub>1g</sub> peaks of the MoS<sub>2</sub> and the G peak of the graphene.

**Density Functional Theory Calculation of the Electronic Structures:** We performed self-consistent DFT calculations with the open-source software Quantum-Espresso.<sup>[39]</sup> For graphene, we used a scalar relativistic, norm-conserving pseudopotential (NCPP), which uses a direct-fit Von Barth-Car method with a Perdew-Zunger (LDA) exchange-correlation functional. For MoS<sub>2</sub>, we used a nonrelativistic NCPP for Mo and a scalar relativistic NCPP for S. Both potentials employed a Martins-Troullier method with a Perdew-Wang (LDA) exchange correlation. The lattice constants are  $a = 2.459$  Å for graphene and  $a = 3.125$  Å,  $z = 3.11$  Å for MoS<sub>2</sub>, where  $z$  is the S-S distance. The band structures produced by these parameters can be found in Figure S13 (Supporting Information). To capture

the monolayer band structure, planes of single-layer graphene or trilayered MoS<sub>2</sub> are separated by a 20 Å vacuum. The cutoff energy for plane waves was 120 Ry for graphene and 140 Ry for MoS<sub>2</sub>. We used a convergence threshold of 10<sup>-16</sup> on a Monkhorst-Pack grid sizes of 8 × 8 × 1 for graphene and 6 × 6 × 4 for MoS<sub>2</sub> for the initial total energy calculation and then performed a bands calculation on a dense grid of 126 040 k-points with a convergence threshold of 10<sup>-12</sup>. We used the central difference method to obtain the band velocities per band which in turn is used to determine the electronic DOS and other transport properties including interfacial transmission and resistance of the interface.

**Mobility Calculation in MoS<sub>2</sub>:** The carrier mobility in graphene, which depends on its carrier concentration, is taken from the work by Dorgan et al.<sup>[47]</sup> In addition to intrinsic phonon-limited carrier mobility in MoS<sub>2</sub> ( $\mu_{ph} \approx 410$  cm<sup>2</sup> V<sup>-1</sup> s<sup>-1</sup>),<sup>[48]</sup> the mobility was also influenced by factors like charged impurities, surface optical (SO) phonons, and other short-range scattering mechanisms. However, it has been reported that the electron mobility in MoS<sub>2</sub> is largely affected by the charged-impurity (CI) scattering.<sup>[49–51]</sup> An empirical expression for CI-limited mobility for MoS<sub>2</sub> has been adopted and modified from the work by Ma and Jena<sup>[51]</sup> and is

given as: 
$$\mu_{CI} \approx \frac{45}{n_{imp}/10^{11} \text{ cm}^{-2}} \left( A(\epsilon) + \left( \frac{C_{oxide} V_g + n_{imp}}{10^{13} \text{ cm}^{-2}} \right)^{1.2} \right),$$
 where

$A(\epsilon) = 0.036$  is a fitting constant depending on the dielectric constant of SiO<sub>2</sub> (oxide layer),  $C_{oxide}$  is the capacitance per unit area of the gate oxide, and  $n_{imp}$  is the charged-impurity density. The impurity density equals sheet charge density ( $n_c = C_{oxide} V_g + n_{imp}$ ) at zero gate voltage. We used an impurity concentration of  $5.5 \times 10^{11}$  cm<sup>-2</sup>, which is found by fitting the finite resistance at zero-gate voltage obtained from experimentally measured  $I_d - V_{ds}$  data. In the presence of multiple scattering mechanisms, the mobility of the free carriers can be represented by Matthiessen's rule and is given as:  $\mu_{MoS_2} = (\mu_{ph}^{-1} + \mu_{CI}^{-1} + \mu_{SR}^{-1})^{-1}$ , where  $\mu_{SR}$  is the mobility due to short-range effects.<sup>[50]</sup>

## Supporting Information

Supporting Information is available from the Wiley Online Library or from the author.

## Acknowledgements

A.S.K. and Z.A. work were supported by National Science Foundation 2-DARE program (Grant # NSF EFMA-1542864). V.K.S. and M.C.H. acknowledge support from the 2-DARE program (NSF EFRI-1433510). A.S.K. acknowledges the MRSEC Materials Preparation and Measurement Laboratory shared user facility at the University of Chicago (Grant# NSF DMR-1420709). R.S.Y. and F.L. acknowledge the funding from National Science Foundation (Grant # NSF CMMI-1619743). A.S.K. and A.B. conceived the idea. A.S.K. led the material synthesis, device fabrications, electrical measurements, and device characterizations. A.B. synthesized the MoS<sub>2</sub>-graphene lateral heterostructure and performed electrical experiments. A.B.

and P.Y. carried out device fabrications and characterizations. P.Y. and T.F. synthesized the CVD graphene. A.K.M. performed band structure alignment, mobility, and interfacial resistance calculations. V.K.S. performed  $1/f$  noise and breakdown measurements and analysis. C.J.F. carried out DFT and transmission coefficient calculations. Z.A. conceived and supervised the calculations. M.C.H. supervised the  $1/f$  noise and breakdown measurements and analysis. F.L. performed KPFM measurements and R.S.Y. supervised him. S.F. helped in DFT calculations. M.R.H. helped in CVD MoS<sub>2</sub> and graphene synthesis. The lead authors acknowledge the assistance of Dr. Daniel P. Bailey in copy-editing this manuscript.

## Conflict of Interest

The authors declare no conflict of interest.

- [1] G. E. Moore, *IEEE Solid-State Circuits Soc. Newsl.* **2006**, *20*, 36.
- [2] S. Najmaei, Z. Liu, W. Zhou, X. Zou, G. Shi, S. Lei, B. I. Yakobson, J.-C. Idrobo, P. M. Ajayan, J. Lou, *Nat. Mater.* **2013**, *12*, 754.
- [3] Y. Zhan, Z. Liu, S. Najmaei, P. M. Ajayan, J. Lou, *Small* **2012**, *8*, 966.
- [4] P. Yasaei, B. Kumar, T. Foroozan, C. Wang, M. Asadi, D. Tuschel, J. E. Indacochea, R. F. Klie, A. Salehi-Khojin, *Adv. Mater.* **2015**, *27*, 1887.
- [5] Y. Zhang, Y. Zhang, Q. Ji, J. Ju, H. Yuan, J. Shi, T. Gao, D. Ma, M. Liu, Y. Chen, X. Song, H. Y. Hwang, Y. Cui, Z. Liu, *ACS Nano* **2013**, *7*, 8963.
- [6] X. Li, W. Cai, J. An, S. Kim, J. Nah, D. Yang, R. Piner, A. Velamakanni, I. Jung, E. Tutuc, S. K. Banerjee, L. Colombo, R. S. Ruoff, *Science* **2009**, *324*, 1312.
- [7] F. Xia, H. Wang, Y. Jia, *Nat. Commun.* **2014**, *5*, 4458.
- [8] Q. H. Wang, K. Kalantar-Zadeh, A. Kis, J. N. Coleman, M. S. Strano, *Nat. Nanotechnol.* **2012**, *7*, 699.
- [9] R. Ganatra, Q. Zhang, *ACS Nano* **2014**, *8*, 4074.
- [10] B. Radisavljevic, A. Radenovic, J. Brivio, V. Giacometti, A. Kis, *Nat. Nanotechnol.* **2011**, *6*, 147.
- [11] S. Das, H. Y. Chen, A. V. Penumatcha, J. Appenzeller, *Nano Lett.* **2013**, *13*, 100.
- [12] R. Kappera, D. Voiry, S. E. Yalcin, B. Branch, G. Gupta, A. D. Mohite, M. Chhowalla, *Nat. Mater.* **2014**, *13*, 1128.
- [13] L. Yu, Y. H. Lee, X. Ling, E. J. G. Santos, Y. C. Shin, Y. Lin, M. Dubey, E. Kaxiras, J. Kong, H. Wang, T. Palacios, *Nano Lett.* **2014**, *14*, 3055.
- [14] Y. Liu, H. Wu, H.-C. Cheng, S. Yang, E. Zhu, Q. He, M. Ding, D. Li, J. Guo, N. O. Weiss, Y. Huang, X. Duan, *Nano Lett.* **2015**, *15*, 3030.
- [15] J. Yoon, W. Park, G. Y. Bae, Y. Kim, H. S. Jang, Y. Hyun, S. K. Lim, Y. H. Kahng, W. K. Hong, B. H. Lee, H. C. Ko, *Small* **2013**, *9*, 3295.
- [16] X. Cui, G.-H. Lee, Y. D. Kim, G. Arefe, P. Y. Huang, C. Lee, D. A. Chenet, X. Zhang, L. Wang, F. Ye, F. Pizzocchero, B. S. Jessen, K. Watanabe, T. Taniguchi, D. A. Muller, T. Low, P. Kim, J. Hone, *Nat. Nanotechnol.* **2015**, *10*, 534.
- [17] W. J. Yu, Z. Li, H. Zhou, Y. Chen, Y. Wang, Y. Huang, X. Duan, *Nat. Mater.* **2012**, *12*, 246.
- [18] P. Yasaei, B. Kumar, R. Hantehzadeh, M. Kayyalha, A. Baskin, N. Reppin, C. Wang, R. F. Klie, Y. P. Chen, P. Král, A. Salehi-Khojin, *Nat. Commun.* **2014**, *5*, 4911.
- [19] P. Yasaei, A. Fathizadeh, R. Hantehzadeh, A. K. Majee, A. El-Ghandour, D. Estrada, C. Foster, Z. Aksamija, F. Khalili-Araghi, A. Salehi-Khojin, *Nano Lett.* **2015**, *15*, 4532.
- [20] X. Ling, Y. Lin, Q. Ma, Z. Wang, Y. Song, L. Yu, S. Huang, W. Fang, X. Zhang, A. L. Hsu, Y. Bie, Y.-H. Lee, Y. Zhu, L. Wu, J. Li, P. Jarillo-Herrero, M. S. Dresselhaus, T. Palacios, J. Kong, *Adv. Mater.* **2016**, *28*, 2322.
- [21] S. Jin-Hong Park, S. Lee, J. Jeon, S. Kyu Jang, S. Min Jeon, G. Yoo, Y. Hee Jang, J.-H. Park, *Nanoscale* **2015**, *7*, 1688.
- [22] H. Liu, M. Si, S. Najmaei, A. T. Neal, Y. Du, P. M. Ajayan, J. Lou, P. D. Ye, *Nano Lett.* **2013**, *13*, 2640.
- [23] J. R. Chen, P. M. Odenthal, A. G. Swartz, G. C. Floyd, H. Wen, K. Y. Luo, R. K. Kawakami, *Nano Lett.* **2013**, *13*, 3106.
- [24] S. Ghatak, A. N. Pal, A. Ghosh, *ACS Nano* **2011**, *5*, 7707.
- [25] S. Adam, S. D. Sarma, *Phys. Rev. B: Condens. Matter Mater. Phys.* **2008**, *77*, 1.
- [26] V. K. Sangwan, H. N. Arnold, D. Jariwala, T. J. Marks, L. J. Lauhon, M. C. Hersam, *Nano Lett.* **2013**, *13*, 4351.
- [27] S. Ghatak, S. Mukherjee, M. Jain, D. D. Sarma, A. Ghosh, *APL Mater.* **2014**, *2*, 92515.
- [28] X. Xie, D. Sarkar, W. Liu, J. Kang, O. Marinov, M. J. Deen, K. Banerjee, *ACS Nano* **2014**, *8*, 5633.
- [29] J. Renteria, R. Samnakay, S. L. Rumyantsev, C. Jiang, P. Goli, M. S. Shur, A. A. Balandin, *Appl. Phys. Lett.* **2014**, *104*, 153104.
- [30] D. Sharma, M. Amani, A. Motayed, P. B. Shah, A. G. Birdwell, S. Najmaei, P. M. Ajayan, J. Lou, M. Dubey, Q. Li, A. V. Davydov, *Nanotechnology* **2014**, *25*, 155702.
- [31] H. J. Kwon, H. Kang, J. Jang, S. Kim, C. P. Grigoropoulos, *Appl. Phys. Lett.* **2014**, *104*, 83110.
- [32] D. Sharma, M. Amani, A. Motayed, P. B. Shah, A. G. Birdwell, S. Najmaei, P. M. Ajayan, J. Lou, M. Dubey, Q. Li, A. V. Davydov, *Nanotechnology* **2014**, *25*, 155702.
- [33] H. N. Arnold, V. K. Sangwan, S. W. Schmucker, C. D. Cress, K. A. Luck, A. L. Friedman, J. T. Robinson, T. J. Marks, M. C. Hersam, *Appl. Phys. Lett.* **2016**, *108*, 073108.
- [34] A. N. Pal, S. Ghatak, V. Kochat, A. Sampathkumar, S. Raghavan, A. Ghosh, *ACS Nano* **2011**, *5*, 2075.
- [35] D. Lembke, A. Kis, *ACS Nano* **2012**, *6*, 10070.
- [36] A. A. Kistanov, Y. Cai, Y.-W. Zhang, S. V. Dmitriev, K. Zhou, *J. Phys.: Condens. Matter* **2017**, *29*, 95302.
- [37] X. Liu, Z. Li, *J. Phys. Chem. Lett.* **2015**, *6*, 3269.
- [38] J. Zhang, W. Xie, J. Zhao, S. Zhang, *2D Mater.* **2016**, *4*, 15038.
- [39] P. Giannozzi, S. Baroni, N. Bonini, M. Calandra, R. Car, C. Cavazzoni, D. Ceresoli, G. L. Chiarotti, M. Cococcioni, I. Dabo, A. Dal Corso, S. de Gironcoli, S. Fabris, G. Fratesi, R. Gebauer, U. Gerstmann, C. Gougousis, A. Kokalj, M. Lazzeri, L. Martin-Samos, N. Marzari, F. Mauri, R. Mazzarello, S. Paolini, A. Pasquarello, L. Paulatto, C. Sbraccia, S. Scandolo, G. Sclauzero, A. P. Seitsonen, A. Smogunov, P. Umari, R. M. Wentzcovitch, *J. Phys.: Condens. Matter* **2009**, *21*, 395502.
- [40] H. Yu, A. Kutana, B. I. Yakobson, *Nano Lett.* **2016**, *16*, 5032.
- [41] Z. Lin, A. McCreary, N. Briggs, W. Zhang, Q. Wang, Y. Chen, A. Kumar, P. K. Ahluwalia, S. Zhu, Y. Ni, J. Liu, B. Ha Nguyen, V. Hieu Nguyen, B. Ram, A. Manjanath, A. K. Singh, J. Sophia Ponraj, Z.-Q. Xu, S. Chander Dhanabalan, Z.-K. Tang, C.-J. Tong, W. Geng, X. Qian, Y. Wang, W. Li, C. Zhang, C. Gong, Y. Nie, K.-A. Min, C. Liang, Y. Jun Oh, H. Zhang, W. Wang, S. Hong, L. Colombo, R. M. Wallace, K. Cho, *2D Mater.* **2017**, *4*, 15026.
- [42] O. V. Zazyev, S. G. Louie, *Nat. Mater.* **2010**, *9*, 806.
- [43] G. Chen, In *Nanoscale Energy Transport and Conversion*. (Ed. 1st), Oxford: New York, **2005**, p. 170.
- [44] G. Gilat, L. J. Raubenheimer, *Phys. Rev.* **1966**, *144*, 390.

- [45] P. Abbasi, M. Asadi, C. Liu, S. Sharifi-Asl, B. Sayahpour, A. Behranginia, P. Zapol, R. Shahbazian-Yassar, L. A. Curtiss, A. Salehi-Khojin, *ACS Nano* **2017**, *11*, 453.
- [46] A. Behranginia, M. Asadi, C. Liu, P. Yasaei, B. Kumar, P. Phillips, T. Foroozan, J. C. Waranius, K. Kim, J. Abiade, R. F. Klie, L. A. Curtiss, A. Salehi-Khojin, *Chem. Mater.* **2016**, *28*, 549.
- [47] V. E. Dorgan, M.-H. Bae, E. Pop, *Appl. Phys. Lett.* **2010**, *97*, 82112.
- [48] K. Kaasbjerg, K. S. Thygesen, K. W. Jacobsen, *Phys. Rev. B* **2012**, *85*, 115317.
- [49] Z. Yu, Z.-Y. Ong, Y. Pan, Y. Cui, R. Xin, Y. Shi, B. Wang, Y. Wu, T. Chen, Y.-W. Zhang, G. Zhang, X. Wang, *Adv. Mater.* **2016**, *28*, 547.
- [50] Z. Yu, Y. Pan, Y. Shen, Z. Wang, Z.-Y. Ong, T. Xu, R. Xin, L. Pan, B. Wang, L. Sun, J. Wang, G. Zhang, Y. W. Zhang, Y. Shi, X. Wang, *Nat. Commun.* **2014**, *5*, 5290.
- [51] N. Ma, D. Jena, *Phys. Rev. X* **2014**, *4*, 11043.

Received: December 29, 2016

Revised: April 24, 2017

Published online: June 19, 2017